東北大学機関リポジトリ
TOUR
Tohoku University Repository

Scaling study of potential in the end region of a tandem mirror based on end-loss electron measurement

著者	Saito T., Kiwamoto Y., Kurihara K., Cho T., Inutake M., Miyoshi S., Tamano T., Yatsu K.
journal or publication title	Physics of fluids. B, Plasma physics
volume	5
number	3
page range	866-871
year	1993-03
URL	http://hdl.handle.net/10097/47826

doi: 10.1063/1.860937

Scaling study of potential in the end region of a tandem mirror based on end-loss electron measurement

T. Saito, Y. Kiwamoto, K. Kurihara, T. Cho, M. Inutake, S. Miyoshi, T. Tamano, and K. Yatsu
Plasma Research Center, University of Tsukuba, Tsukuba City, Ibaraki 305, Japan

(Received 18 June 1992; accepted 13 November 1992)

An empirical scaling for the potential difference between the plug potential Φ_P and the floating potential Φ_{EP} of an endplate is obtained in terms of end-loss electron temperatures. Results from the GAMMA 10 tandem mirror [Phys. Rev. Lett. **55**, 939 (1985)] indicate that $\Delta\Phi=\Phi_P-\Phi_{EP}$ scales much better with an effective temperature $T_{\text{eff}}\equiv(1-\beta)T_{eL}+\beta T_{eH}$ than with a single temperature T_{eL} or T_{eH}, where T_{eL} and T_{eH} are temperatures of the bulk and the high-energy tail components of the end-loss electrons and β denotes the flux fraction of the T_{eH} component. Moreover, the observed scaling is consistent with a recently developed theoretical model [K. Kurihara *et al.*, J. Phys. Soc. Jpn. **61**, 3153 (1992)].

I. INTRODUCTION

The basis for plasma confinement in a tandem mirror is a properly tailored potential profile along magnetic field lines, and extensive studies have been performed in order to understand the mechanism of potential formation. Major efforts have been placed on the studies of internal structure, depth of the thermal barrier[1,2] and ion-confining potential,[3,4] etc. However, the potential difference $\Delta\Phi$ between the confinement region and the end wall is also an important factor for complete understanding of the tandem mirror potential. In this paper an empirical scaling study of $\Delta\Phi$ is described based on a data set accumulated on the GAMMA 10 tandem mirror.[5]

Fundamental electron cyclotron resonance heating (ECRH) is used for formation of the confining potential in current tandem mirrors and it induces an intense end-loss flux of warm electrons.[6,7] The warm electron flux gives rise to two important features in the process of $\Delta\Phi$ formation. First, $\Delta\Phi$ becomes much larger than that expected from the ambipolar condition between confined electrons and ions[8,9] and, moreover, $\Delta\Phi$ sensitively depends on the energy spectrum of the end-loss electrons. Second, secondary electrons emitted from the end wall affect the simple ambipolar condition.[10]

There have been a few basic experiments and simulation studies on the effects of an electron-emissive end wall.[11–13] A scaling study on tandem mirror potentials has also been carried out,[14] but the main subject of this study is statistical correlations between the potentials and other parameters, i.e., the electron densities and the ECRH power. This paper provides the first explicit discussions on the elements of the potential difference $\Delta\Phi$. In particular, it deals with measurement of end-loss electrons and application of a recently developed theoretical model, which includes effects of the energy spectrum of the end-loss electrons, the secondary electrons emitted from the endplate, and the variation of the magnetic field strength along a field line. This study gives a clue for a more complete understanding of the tandem mirror potential.

Section II gives a brief description of the experimental setup. Also presented in Sec. II is the empirical scaling of potential in the end region of GAMMA 10 in terms of end-loss electron measurement. Section III is devoted to explanation of the main point of the models; then, comparison of the scaling with the model is made. Finally, Sec. IV summarizes the present study.

II. SCALING OF POTENTIAL IN THE END REGION

Both the plug and the thermal barrier potentials are formed in an axisymmetric end mirror cell by using ECRH.[5] The end region extends from the mirror throat of the end cell to an endplate as shown in Fig. 1. The endplate is installed for reduction of the nonambipolar diffusion.[15] The magnetic field strength varies from 3.0 T at the mirror throat to about 0.01 T on the endplate. The endplate is made of stainless steel and radially divided into five concentric plates. Each plate is connected to the vacuum vessel through a high resistance and hence it is virtually floating.

Characteristics of the end-loss electrons are diagnosed with a multigrid energy analyzer called LED (loss electron diagnostics),[7] installed behind the endplate. Loss electrons are measured through a small hole in the plate. Two LED's are used and the radial positions of LED's correspond to 2.8 and 6.4 cm in radius at the plug position along the magnetic field line. The plug potential Φ_P is measured by an end-loss analyzer (ELA).[16] Potentials at the central cell and the barrier midplane are measured by beam probes[17] and those in front of the endplate are measured by a Langmuir probe.

Upon application of the fundamental ECRH to the plasma in the end mirror cell (which is produced mainly by second harmonic ECRH), a high ion confining potential is formed as shown in Fig. 1. Consequently, the ion end-loss flux is strongly suppressed.[16] In this paper we discuss the difference $\Delta\Phi$ between the plug potential Φ_P (>0) and the floating potential Φ_{EP}(<0) of the endplate. The formation of the high plasma potentials is accompanied by an axial flow of warm electrons.[6]

 0899-8221/93/030866-06$06.00 © 1993 American Institute of Physics

Downloaded 06 Apr 2010 to 130.34.135.83. Redistribution subject to AIP license or copyright; see http://pop.aip.org/pop/copyright.jsp

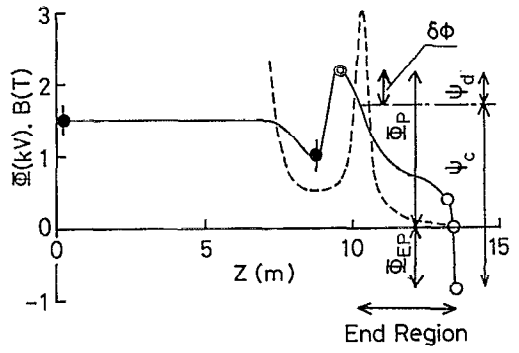

FIG. 1. An example of the axial potential profile when the fundamental ECRH is turned on. The potential profile from the central cell midplane to the endplate is shown. Potentials on the same magnetic field line are measured by the beam probes (●), the ELA (◎), and the Langmuir probe (○). The potential of the vacuum vessel is referred to zero. Normalized potentials ψ_d and ψ_c appearing in the theoretical model are also indicated. They are measured from the potential at the mirror throat. The magnetic field profile in the end region is plotted by the dashed line.

We have first measured the characteristics of the end-loss electrons with the LED. The end-loss electron flux to the LED is plotted in Fig. 2 as a function of the bias voltage $-V_{ER}$ ($V_{ER}>0$) applied to the electron retarding grid of the LED. Here, V_{ER} is measured from the vacuum vessel. The loss flux is well approximated by

$$I_e = I_L \exp\left[-\left(\frac{V_{ER}+\Phi_{EP}}{T_{eL}}\right)\right] + I_H \exp\left[-\left(\frac{V_{ER}+\Phi_{EP}}{T_{eH}}\right)\right]$$

for $V_{ER} \geq -\Phi_{EP}$ as shown by the dashed lines in Fig. 2, which is characterized by three parameters, namely, the

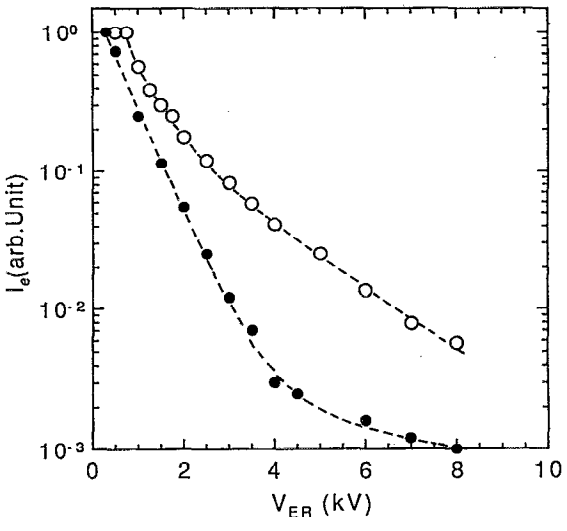

FIG. 2. Energy spectra of the end-loss electrons measured by an LED. The ordinate is the normalized loss electron flux as a function of the electron retarding voltage V_{ER} of the LED. The dashed lines stand for the flux created from the best-fit two component Maxwellian. Two typical cases are shown, i.e., the high-β case (○): $\Phi_{EP}=0.75$ kV, $T_{eL}=0.52$ keV, $T_{eH}=2.1$ keV, $\beta=0.18$, $T_{\rm eff}=0.80$ keV; and the low-β case (●): $\Phi_{EP}=0.3$ kV, $T_{eL}=0.58$ keV, $T_{eH}=6.4$ keV, $\beta=0.0034$, $T_{\rm eff}=0.60$ keV. The parameters T_{eL}, T_{eH}, I_L, and I_H are determined by using least-square fitting. Then β is defined as $I_H/(I_L+I_H)$.

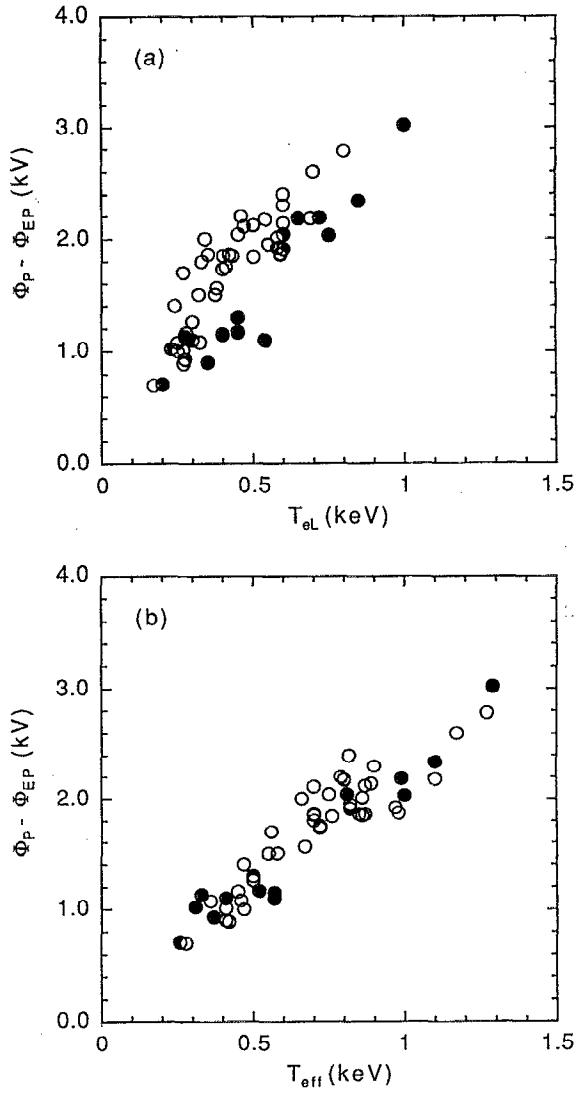

FIG. 3. Scaling plots of the potential difference $\Delta\Phi$. (a) $\Delta\Phi$ as a function of the end-loss electron temperature T_{eL} of the bulk component; (b) $\Delta\Phi$ as a function of the effective temperature $T_{\rm eff}$. The closed circles represent data with $T_{\rm eff}<1.4T_{eL}$.

temperature of the bulk component T_{eL}, that of the higher energy tail component T_{eH}, and the flux fraction of the T_{eH} component $\beta \equiv I_H/(I_L+I_H)$, where I_L and I_H are fluxes of the two components, respectively. These parameters vary depending on the ECRH power, the densities at the central cell and the end mirror cell, the radial position, etc. Figure 2 represents two typical examples of the end-loss electron flux with nearly the same T_{eL} but with different β: a high-β case and a low-β case.

Most of the loss flux belongs to the bulk component even for the high-β case, and the value of $\Delta\Phi=\Phi_P-\Phi_{EP}$ is typically three to four times T_{eL}. As the first step, it may be considered that $\Delta\Phi$ is solely determined by T_{eL}. Figure 3(a) plots $\Delta\Phi$ as a function of T_{eL}. A positive correlation is certainly seen. However, plotted points still scatter considerably and each T_{eL} does not uniquely correspond to $\Delta\Phi$. This implies that there are other important parameters which are not taken into account in Fig. 3(a).

Downloaded 06 Apr 2010 to 130.34.135.83. Redistribution subject to AIP license or copyright; see http://pop.aip.org/pop/copyright.jsp

As shown in Fig. 2, the T_{eH} component does not always have the same fraction β for the same T_{eL}. A recently developed theoretical model suggests that the T_{eH} component cannot be neglected in determining $\Delta\Phi$ and even a small fraction of this component affects $\Delta\Phi$.[18] Therefore, it is necessary to include the T_{eH} component as the second step. We define an effective temperature $T_{\rm eff} \equiv (1-\beta)T_{eL}+\beta T_{eH}$. Closed circles in Fig. 3(a) stand for data with $T_{\rm eff} < 1.4T_{eL}$ corresponding to low β roughly less than 0.1. This indicates that the major cause of scattering of the plotted points is β. Figure 3(b) shows $\Delta\Phi$ as a function of $T_{\rm eff}$. It is seen that $\Delta\Phi$ is much better represented by $T_{\rm eff}$ than by T_{eL}. The temperature of the higher energy component T_{eH} is typically four to seven times T_{eL}, but β varies considerably, from less than 1% to more than 20% depending on the experimental conditions. The value of $T_{\rm eff}$ is twice as much as T_{eL} for β of 0.2. The systematic deviation between the open circles and the closed circles for the same T_{eL} in Fig. 3(a) is thereby removed by the introduction of $T_{\rm eff}$.

III. COMPARISON OF THE SCALING WITH A MODEL AND DISCUSSION

Figure 3(b) indicates that $T_{\rm eff}$ should better represent physical reality. We examined the data referring to the theoretical model[18] which can be directly applied to the present situation. Here, we describe the main point of the model. It considers the axial potential profile between the outer mirror throat $B=B_a$ (3.0 T) and the endplate $B=B_c$ (0.01 T) (see Fig. 1). The potential ϕ at the mirror throat is defined as the reference to be zero. The floating endplate potential is ϕ_c. Particle species included in the model are end-loss electrons composed of two components, loss ions and secondary electrons emitted from the end wall. All of those are assumed to have truncated Maxwellian distributions, and collisions are neglected. Since the potential peak is presumably created inside the mirror throat, the ions have a drift energy ϵ_d at the mirror throat due to acceleration by the potential drop between the plug to the mirror throat.

The distribution functions of the ions and electrons satisfy the Vlasov equation. Thus we can express the distribution functions with the constants of motion, the energy ϵ, and the magnetic moment μ. The energy of an ion is $\epsilon=(1/2)M(v_\perp^2+v_\parallel^2)+e\phi$, where M is the ion mass, e is the unit charge ($e>0$), and $v_\perp$ and $v_\parallel$ are the perpendicular and parallel components of velocity. The magnetic moment is $\mu=(1/2)Mv_\perp^2/B$. The distribution function of ions coming out of the mirror throat is given by

$$f_i(\epsilon)=N_{i0}\left(\frac{M}{2\pi T_i}\right)^{3/2}\exp\left(\frac{-(\epsilon-\epsilon_d)}{T_i}\right). \tag{1}$$

End-loss ions are bounded in the hatched region of the ϵ-μ space as shown in Fig. 4(a). The electron and secondary electron distribution functions are similarly given as

$$f_e(\epsilon)=N_{e0}\left(\frac{m}{2\pi T_e}\right)^{3/2}\exp\left(-\frac{\epsilon}{T_e}\right), \tag{2}$$

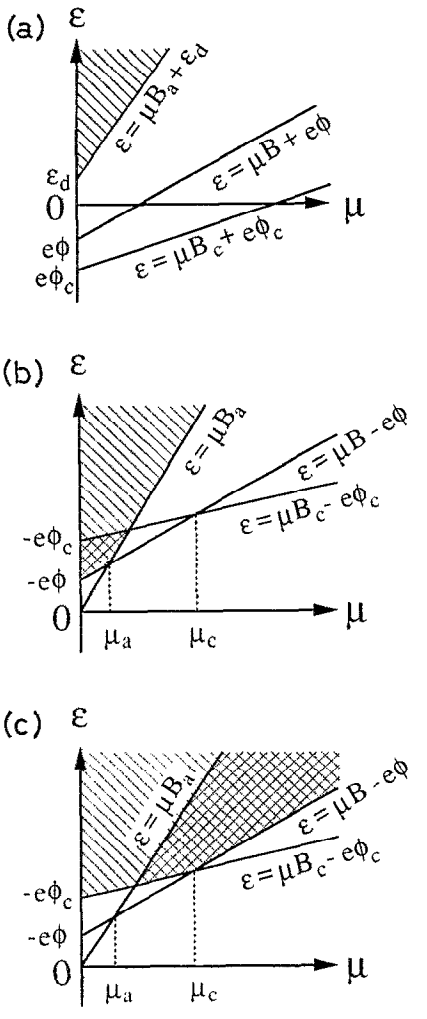

FIG. 4. Energy-magnetic moment space of the ions (a), th primary electrons (b), and the secondary electrons (c). Here, ϵ and μ are the energy and the magnetic moment. Particles in the hatched region pass through the model region and those in the checkered region are reflected, where $\mu_a<\mu_c$.

$$f_{se}(\epsilon)=N_{se0}\left(\frac{m}{2\pi T_{se}}\right)^{3/2}\exp\left(-\frac{\epsilon}{T_{se}}\right), \tag{3}$$

where m is the electron mass and the electron energy is $\epsilon=(1/2)m(v_\perp^2+v_\parallel^2)-e\phi$. The subscripts i, e, and se denote ions, electrons, and secondary electrons, respectively. Here, N_{i0}, N_{e0}, and N_{se0} are densities of the full Maxwellian sources of each species. The regions in which the primary electrons and the secondary electrons exist are bounded in the hatched and checkered regions in Fig. 4(b) and 4(c). Though only the expressions for a single-temperature electron distribution are given here for the sake of simplicity, it is easy to extend to the case of two electron temperature components.

Integration of each distribution function yields the corresponding density as a function of the normalized potential ψ and the magnetic field B as given in the Appendix. The following nondimensional variables are used:

Downloaded 06 Apr 2010 to 130.34.135.83. Redistribution subject to AIP license or copyright; see http://pop.aip.org/pop/copyright.jsp

$$\psi=e\phi/T_{eL},\quad \tau=T_i/T_{eL},\quad \sigma=T_{se}/T_{eL},$$

$$\alpha=T_{eH}/T_{eL},\quad \beta=I_H/(I_H+I_L),\quad \psi_d=\epsilon_d/T_{eL}.$$

Here, I_H and I_L are the net fluxes of the higher and lower temperature electrons which reach the endplate. The flux of ions flowing into the endplate per the magnetic flux tube is given as

$$I_i=\frac{2\pi B_c}{M^2}\int_0^\infty d\mu\int_{\epsilon_d}^\infty d\epsilon\, f_i(\epsilon,\mu)=N_{i0}\frac{B_c}{B_a}\left(\frac{\tau T_{eL}}{2\pi M}\right)^{1/2}. \tag{4}$$

It is constant throughout the region. The fluxes of the electrons and secondary electrons are similarly given as

$$I_e=N_{e0}\left(\frac{T_{eL}}{2\pi m}\right)^{1/2}\left[\exp(\psi_c)+\left(\frac{B_c}{B_a}-1\right)\exp\left(\frac{B_a\psi_c}{B_a-B_c}\right)\right] \tag{5}$$

and

$$I_{se}=N_{se}\left(\frac{\sigma T_{eL}}{2\pi m}\right)^{1/2}\exp\left(\frac{\psi_c}{\sigma}\right). \tag{6}$$

The fluxes of the electrons are related by $I_{sc}=-\gamma I_e$, where γ is the secondary electron emission coefficient. The floating condition of the endplate is $I_i=I_e+I_{se}$, which relates the endplate potential ψ_c with the density ratios N_{se0}/N_{i0} and N_{e0}/N_{i0}. By imposing the charge neutrality condition at the mirror throat, ψ_c is determined.

The end region is divided into the plasma region out of the mirror throat and the sheath region in front of the endplate. In the plasma region between the outer mirror throat and the sheath region, the charge neutrality equation

$$N_i(B,\psi)-N_e(B,\psi)-N_{se}(B,\psi)=0 \tag{7}$$

is employed for calculation of the potential profile. Here, the space charge is neglected but the effect of the magnetic field variation is taken into consideration because the magnetic field decreases from 3.0 T to 0.014 T while the scale length of the spatial variation is much larger than the local Debye length. The solution at $B=B_a-\Delta B$ near the mirror throat does not always connect smoothly to $\psi=0$ as $\Delta B/B$ goes to zero and a stepwise potential drop appears. However, there is a unique value of the ion-drift energy ψ_d which leads to a smooth solution at $B=B_a$. The potential can be connected in a few Debye lengths when we solve Poisson's equation. This indicates that if we do not consider a correct amount of the ion drift, we have to introduce a source sheath, where the charge neutrality is not satisfied. In this model ψ_d is regarded as the potential drop from the plug to the mirror throat.

Near the endplate, the axial scale length of the potential is comparable with the Debye length (typically a few cm). Thus, the potential is calculated from the one-dimensional Poisson equation in the sheath region,

$$\frac{d^2\psi}{dz^2}=-\frac{e^2}{\epsilon_0 T_{eL}}[N_i(B,\psi)-N_e(B,\psi)-N_{se}(B,\psi)]. \tag{8}$$

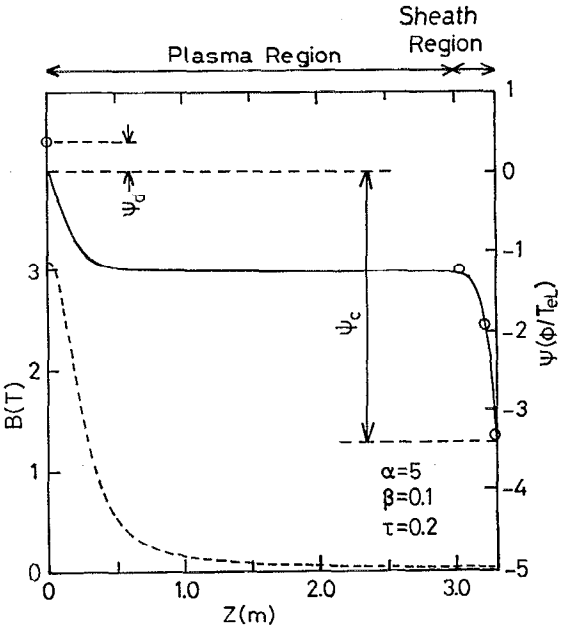

FIG. 5. An example of the calculated potential profile (solid line) for $\gamma_L=0.65$, $\gamma_H=0.5$, $\sigma=0.01$, $N_{i0}=1\times10^{11}$ cm^{-3}. The potential ψ is normalized as $e\phi/T_{eL}$. The open circles stand for the potential measured by the Langmuir probe. The magnetic field profile is also plotted with the dashed line. The origin of the z axis is located at the mirror throat, which is different from that of Fig. 1.

Here, ϵ_0 is the dielectric constant in the vacuum. Because the variation of the magnetic field is from 0.014 T to 0.01 T, we neglect the effect of the divergent magnetic field.

The velocity distributions of ions, electrons, and secondary electrons should change continuously at the transition from the plasma region to the sheath region. Thus the potential and the densities should be continuously connected at the transition. The position of the transition is determined so that the potential drop in the plasma region plus the sheath potential is equal to ψ_c. The electric field and the densities calculated in the plasma region are used as the initial values of the differential equation.

A detailed analysis of the model is provided in Ref. 18. Thus we show a typical example of the potential profile calculated with the model. Figure 5 plots the normalized potential profile in the end region, which is similar to the experimentally observed potential distribution. There is a steep potential drop in front of the endplate, which is observed by using the Langmuir probe. Since ψ_d is considered to be equal to $e\delta\phi/T_{eL}$, where $\delta\phi$ is the potential drop from the plug to the mirror throat, we compare the theoretically obtained potential drop $\psi_d-\psi_c$ with the experimental result $e\Delta\Phi/T_{eL}$ (see Fig. 1).

Figure 6 shows a comparison of the experimental value with the calculated value. Here, ψ_d and ψ_c are evaluated by using measured parameters: T_{eL}, T_{eH}, β, and the end-loss ion temperature. The effect of secondary electrons is also included in the calculation. The normalized value $\Delta\psi=\Delta\Phi/(\psi_d-\psi_c)T_{eL}$ is plotted as a function of $T_{\rm eff}/T_{eL}$. The value of $\Delta\psi$ lies around unity for various values of $T_{\rm eff}/T_{eL}$, which points out that the calculated potential

Downloaded 06 Apr 2010 to 130.34.135.83. Redistribution subject to AIP license or copyright; see http://pop.aip.org/pop/copyright.jsp

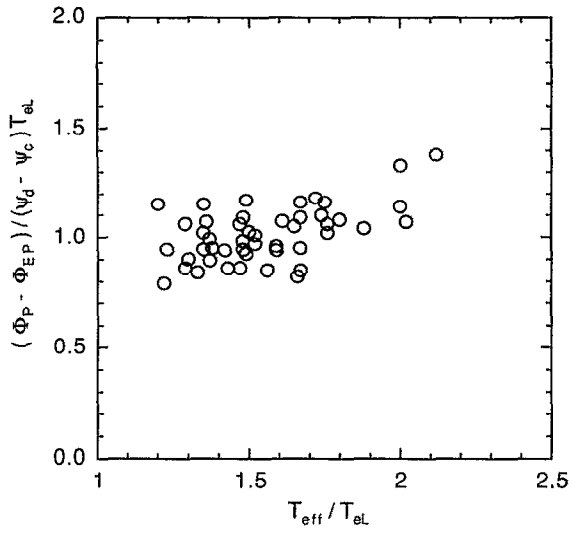

FIG. 6. Comparison between experimental data and the theoretical calculations. Both values are normalized by T_{eL}.

$(\psi_d-\psi_c)T_{eL}$ properly reproduces the measured $\Delta\Phi$. The satisfactory agreement means that the physical picture of the theoretical model developed in Ref. 18 represents the essential factors of the potential in the end region of a tandem mirror in which strong electron heating is employed. Namely, $\Delta\Phi$ is composed of the three major parts, i.e., the potential difference between the plug and the mirror throat, the potential drop due to the magnetic field variation outside the mirror throat, and the sheath potential in front of the floating endplate. They are correctly evaluated by considering the energy spectrum of the end-loss electrons and the secondary electron emission.

The energy spectrum of the end-loss electrons has been measured in a wide energy range up to 20 keV. Another component with a temperature higher than T_{eH} occasionally appears. However, since the fraction of the component is very small (less than 1% at the highest), this component has little effect on the potential. This has been confirmed with the model including three components of end-loss electrons. The energy spectrum itself is also an interesting subject which reflects the diffusion process in velocity space,[19,20] but discussions on it are beyond the scope of this paper.

We have studied $\Delta\Phi$ along a magnetic field line. As a matter of fact, $\Delta\Phi$ at two different radial positions corresponding to the two LED's fits to the same scaling. This implies that the first consideration determining $\Delta\Phi(=\Phi_P-\Phi_{EP})$ is the charge balance on each magnetic field line. Experimentally, Φ_P is positive and it has a radial profile peaking on axis. On the other hand Φ_{EP} is negative and it is minimum on axis. Thus the next problem is the examination of major factors which determine the radial profiles of Φ_P and Φ_{EP} measured from the vacuum vessel. Up to now this has been partly studied from several viewpoints, i.e., the nonambipolar diffusion[16] and the profile of electron heating.[6] However, more comprehensive understanding of the radial potential profile still remains as a future work.

IV. SUMMARY

A scaling for the difference between the plug potential and the floating potential of the endplate is obtained. The difference is nearly proportional to the effective temperature of the end-loss electrons. The significance of the higher temperature component of the end-loss electrons on the potential formation is experimentally pointed out and it is theoretically confirmed.

ACKNOWLEDGMENT

The authors would like to thank the members of the GAMMA 10 group for collaboration and valuable discussions in the course of the present study.

APPENDIX: EXPRESSIONS OF THE ION AND ELECTRON DENSITIES

Expressions of the ion density N_i, the electron density N_e, and the secondary electron density N_{se} are given as follows:

$$N_i(B,\psi)=\frac{1}{2}N_{i0}\left[\exp\left(\frac{\psi_d-\psi}{\tau}\right)\mathrm{erfc}\sqrt{\frac{\psi_d-\psi}{\tau}}-\sqrt{\frac{B_a-B}{B_a}}\exp\left(\frac{B_a}{B_a-B}\frac{\psi_d-\psi}{\tau}\right)\mathrm{erfc}\sqrt{\frac{B_a}{B_a-B}\frac{\psi_d-\psi}{\tau}}\right], \tag{A1}$$

$$N_e(B,\psi)=\frac{1}{2}N_{e0}\exp(\psi)\left(1+\mathrm{erf}\sqrt{\psi-\psi_c}-\sqrt{\frac{B-B_c}{B_c}}\exp(\psi_c-\psi)\left\{D\left(\sqrt{\frac{B_c}{B-B_c}(\psi-\psi_c)}\right)\right.\right.$$
$$\left.\left.-\exp\left(\frac{B_c\psi_c}{B_a-B_c}\right)D\left[\sqrt{\frac{B_c}{B-B_c}\left(\frac{B-B_a}{B_a-B_c}\psi_c+\psi\right)}\right]\right\}$$
$$\left.-\sqrt{\frac{B_a-B}{B_a}}\exp\left(\frac{\psi B}{B_a-B}\right)\left(1+\mathrm{erf}\sqrt{\frac{-B_a\psi_c}{B_a-B_c}+\frac{B_a\psi}{B_a-B}}\right)\right),\quad \text{for } \mu_a\equiv\frac{-\psi}{B_a-B}<\mu_c\equiv\frac{\psi-\psi_c}{B-B_c},$$

Downloaded 06 Apr 2010 to 130.34.135.83. Redistribution subject to AIP license or copyright; see http://pop.aip.org/pop/copyright.jsp

$$=\frac{1}{2}N_{e0}\exp(\psi)\times\left[1+\mathrm{erf}\sqrt{\psi-\psi_c}-\sqrt{\frac{B-B_c}{B_c}}\exp(\psi_c-\psi)D\left(\sqrt{\frac{B_c}{B-B_c}(\psi-\psi_c)}\right)\right.$$

$$\left.-\sqrt{\frac{B_a-B}{B_a}}\exp\left(\frac{\psi B}{B_a-B}\right)\right],\quad \text{for } \mu_a>\mu_c, \tag{A2}$$

$$N_{se}(B,\psi)=\frac{1}{2}N_{se0}\exp\left(\frac{\psi}{\sigma}\right)\left(\mathrm{erfc}\sqrt{\frac{\psi-\psi_c}{\sigma}}+\sqrt{\frac{B_a-B}{B_a}}\exp\left(\frac{B}{B_a-B}\frac{\psi}{\sigma}\right)\mathrm{erfc}\sqrt{\frac{-B_a}{B_a-B_c}\frac{\psi_c}{\sigma}+\frac{B_a}{B_a-B}\frac{\psi}{\sigma}}+\sqrt{\frac{B-B_c}{B_c}}\exp\left(\frac{\psi_c-\psi}{\sigma}\right)\right.$$

$$\left.\times\left\{D\left[\sqrt{\frac{B_c}{B-B_c}\left(\frac{\psi-\psi_c}{\sigma}\right)}\right]+\exp\left(\frac{B_c}{B_a-B_c}\frac{\psi_c}{\sigma}\right)D\left[\sqrt{\frac{B_c}{B-B_c}\left(\frac{B-B_a}{B_a-B_c}\frac{\psi_c}{\sigma}+\frac{\psi}{\sigma}\right)}\right]\right\}\right),\quad \text{for } \mu_a<\mu_c,$$

$$=\frac{1}{2}N_{se0}\exp\left(\frac{\psi}{\sigma}\right)\left[\mathrm{erfc}\sqrt{\frac{\psi-\psi_c}{\sigma}}+\sqrt{\frac{B_a-B}{B_a}}\exp\left(\frac{B}{B_a-B}\frac{\psi}{\sigma}\right)\right.$$

$$\left.+\sqrt{\frac{B-B_c}{B_c}}\exp\left(\frac{\psi_c-\psi}{\sigma}\right)D\left[\sqrt{\frac{B_c}{B-B_c}\left(\frac{\psi-\psi_c}{\sigma}\right)}\right]\right],\quad \text{for } \mu_a>\mu_c, \tag{A3}$$

where erf and erfc are the error function and the complementary error function, respectively, and $D(x)$ stands for the Dawson integral function:[21]

$$D(x)=\frac{2}{\sqrt{\pi}}\exp(-x^2)\int_0^x\exp(t^2)dt.$$

[1] I. Katanuma, Y. Kiwamoto, K. Ishii, and S. Miyoshi, Phys. Fluids **29**, 4138 (1986).
[2] K. Ishii, M. Kotoku, T. Segawa, I. Katanuma, A. Mase, Y. Nakashima, and S. Miyoshi, Nucl. Fusion **30**, 1051 (1990).
[3] P. J. Catto and R. Carrera, Phys. Fluids **26**, 2161 (1983).
[4] R. H. Cohen, Phys. Fluids **26**, 2774 (1983).
[5] M. Inutake, T. Cho, M. Ichimura, K. Ishii, A. Itakura, I. Katanuma, Y. Kiwamoto, Y. Kusama, A. Mase, S. Miyoshi, Y. Nakashima, T. Saito, A. Sakasai, K. Sawada, I. Wakaida, N. Yamaguchi, and K. Yatsu, Phys. Rev. Lett. **55**, 939 (1985).
[6] T. Kariya, T. Saito, Y. Kiwamoto, T. Cho, H. Sugawara, T. Kondoh, A. Mase, A. Itakura, and S. Miyoshi, Phys. Fluids **31**, 1815 (1988).
[7] K. Kurihara, T. Saito, Y. Kiwamoto, and S. Miyoshi, J. Phys. Soc. Jpn. **58**, 3453 (1989).
[8] G. D. Porter, Nucl. Fusion **28**, 1159 (1988).
[9] T. Saito, Y. Kiwamoto, K. Kurihara, T. Honda, A. Kasugai, T. Cho, K. Ishii, I. Katanuma, A. Mase, N. Yamaguchi, and S. Myoshi, in *Abstracts of International Workshop on Strong Microwaves in Plasmas*, 1990, Gorky (Institute of Applied Physics, Gorky, 1990), Abstract H14.
[10] L. S. Hall, Nucl. Fusion **17**, 681 (1977).
[11] C. Chan, H. Bewley, N. Hershkowitz, and J. R. Dekock, Nucl. Fusion **22**, 105 (1982).
[12] K. Sato, F. Miyawaki, and W. Fukui, Phys. Fluids B **1**, 725 (1989).
[13] S. Ishiguro and N. Sato, J. Phys. Soc. Jpn. **60**, 2218 (1991).
[14] G. D. Porter, Nucl. Fusion **29**, 2217 (1989).
[15] I. Katanuma, Y. Kiwamoto, S. Adachi, M. Inutake, K. Ishii, K. Yatsu, K. Sawada, and S. Miyoshi, Nucl. Fusion **27**, 2041 (1987).
[16] T. Cho, M. Inutake, K. Ishii, I. Katanuma, Y. Kiwamoto, A. Mase, Y. Nakashima, T. Saito, N. Yamaguchi, K. Yatsu, M. Hirata, T. Kondoh, H. Sugawara, J. H. Foote, and S. Miyoshi, Nucl. Fusion **28**, 2187 (1988).
[17] K. Ishii, M. Kotoku, T. Segawa, I. Katanuma, A. Mase, and S. Miyoshi, Rev. Sci. Instrum. **60**, 3270 (1989).
[18] K. Kurihara, Y. Kiwamoto, T. Saito, K. Yatsu, and S. Miyoshi, J. Phys. Soc. Jpn. **61**, 3153 (1992).
[19] Y. Kiwamoto, T. Saito, K. Kurihara, I. Katanuma, T. Cho, and S. Miyoshi, in *Nonlinear Dynamics and Particle Acceleration*, Particle and Field Series 45 (American Institute of Physics, New York, 1991), p. 125.
[20] T. Saito, I. Katanuma, Y. Kiwamoto, T. Kariya, and S. Miyoshi, Phys. Rev. Lett. **59**, 2748 (1987).
[21] M. Abramowitz and I. Stegun, *Handbook of Mathematical Functions* (Dover, New York, 1974), p. 319.

Downloaded 06 Apr 2010 to 130.34.135.83. Redistribution subject to AIP license or copyright; see http://pop.aip.org/pop/copyright.jsp